



PCCP

**Spectroscopic Investigations of Electron and Hole Dynamics  
in MAPbBr<sub>3</sub> Perovskite Film and Carrier Extraction to PEDOT  
Hole Transport Layer**

Journal:	<i>Physical Chemistry Chemical Physics</i>
Manuscript ID	CP-ART-02-2021-000658.R2
Article Type:	Paper
Date Submitted by the Author:	27-May-2021
Complete List of Authors:	Niedzwiedzki, Dariusz; Washington University in St Louis, Department of Energy, Environmental & Chemical Engineering Kouhnavard, Mojgan; Washington University in St Louis, Energy, Environmental and Chemical Engineering Diao, Yifan; Washington University in St Louis, Institute of Materials Science & Engineering D'Arcy, Julio; Washington University in St Louis, Department of Chemistry Biswas, Pratim; Washington University in St Louis, Energy, Environmental and Chemical Engineering

SCHOLARONE™  
Manuscripts

# Spectroscopic Investigations of Electron and Hole Dynamics in MAPbBr<sub>3</sub> Perovskite Film and Carrier Extraction to PEDOT Hole Transport Layer

**Dariusz M. Niedzwiedzki<sup>a,b,\*</sup>, Mojgan Kouhnavard<sup>b</sup>, Diao Yifan<sup>c</sup>, Julio M. D'Arcy<sup>c,d</sup>,  
Pratim Biswas<sup>b,\*</sup>**

<sup>a</sup>Center for Solar Energy and Energy Storage, <sup>b</sup>Department of Energy Environmental and Chemical Engineering, <sup>c</sup>Institute of Materials Science & Engineering, <sup>d</sup>Department of Chemistry, Washington University in St. Louis, St. Louis, MO 63130, USA

*\*Corresponding authors emails:*

Dariusz M. Niedzwiedzki: [niedzwiedzki@wustl.edu](mailto:niedzwiedzki@wustl.edu)

Pratim Biswas: [pbiswas@miami.edu](mailto:pbiswas@miami.edu)

**Abstract**

Organometallic halide perovskite (MAPPbBr<sub>3</sub>), Rust-based Vapor Phase Polymerization (RVPP)-PEDOT hole transporting layers and (RVPP-PEDOT)/MAPPbBr<sub>3</sub> dual-layer, deposited on fluorine doped tin oxide glass were studied at room temperature using steady-state absorption, time-resolved photoluminescence imaging and femtosecond time-resolved absorption spectroscopy. Application of these techniques in conjunction with diverse excitation intensities allowed determination of various optoelectronic properties of the perovskite film and the time constant of the hole extraction process. Spectral reconstruction of the bandedge absorption spectrum using Elliot's formula enabled separation of the exciton band. The binding energy of the exciton was determined to be 19 meV and the bandgap energy of the perovskite film was 2.37 eV. Subsequent time-resolved photoluminescence studies of the perovskite film performed using a very weak excitation intensity followed by a global analysis of the data revealed monomolecular recombination dynamics of charge carriers occurring with an amplitude weighted lifetime of 3.2 ns. Femtosecond time-resolved transient absorption of the film performed after excitation intensity spanning a range of over two orders of magnitude enabled determining the rate constant of bimolecular recombination and was found to be  $2.6 \times 10^{-10} \text{ cm}^3 \text{ s}^{-1}$ . Application of numerous high intensity excitations enabled observation of band filling effect and application of the Burstein-Moss model allowed to determine the reduced effective mass of photoexcited electron-hole pair in MAPPbBr<sub>3</sub> film to be 0.19 rest mass of the electron. Finally, application of transient absorption on RVPP-PEDOT/MAPPbBr<sub>3</sub> enabled determination of a 0.4 ps time constant for the MAPPbBr<sub>3</sub>-to-PEDOT hole extraction process.

## Introduction

Perovskite solar cells (PSCs) have attracted tremendous attention as their efficiencies have increased from a few percent in 2009 to 25.2% in 2020.<sup>1</sup> Two main architectures are considered for PSCs depending on a mesoporous or planar morphology of the electron transfer layer (ETL). Planar PSCs have two possible geometries where the perovskite layer is deposited on 1) the ETL or 2) the hole transfer layer (HTL), the latter known as an inverted planar PSC.<sup>2</sup> Among them, the inverted planar structure is more promising for commercialization due to higher cell stability allowing lower processing temperatures and simpler fabrication with negligible hysteresis behavior.<sup>3,4</sup> In a planar inverted structure, the HTL plays an important role in establishing the cell efficiency, as well as stability. Thus, further characterization of the inverted planar structure is necessary. Poly(3,4-ethyl-enedioxythiophene):poly(styrenesulfonate) (PEDOT:PSS) has been shown to be one of the most efficient alternative HTL material to spiro-OMeTAD due to higher thermal stability, electrical conductivity, good optical transparency and suitable energy level alignment with respect to perovskite.<sup>5-7</sup> This polymer is a commercial aqueous formulation developed by hybridizing PEDOT and its counter anion component PSS. PEDOT:PSS HTLs are mainly deposited using solution processing techniques in which the acidic nature of the PEDOT:PSS can cause degradation of the perovskite and top electrode layer.<sup>3</sup> On the other hand, hygroscopic nature of PEDOT:PSS can attract moisture to the perovskite layer resulting in lower stability and poorer performance of PSCs. In addition, low conductivity of PEDOT:PSS due to PSS results in limited charge transport within a PEDOT:PSS layer, and between the PEDOT and perovskite layers thereby increasing the recombination rate and charge accumulation at the interface.<sup>8</sup>

Several attempts have been made to overcome limited charge transport by replacing PEDOT:PSS with an alternative HTL such as NiO<sub>x</sub>.<sup>9</sup> However, given the cost-effectiveness of PEDOT:PSS, current research efforts seek to optimize PEDOT:PSS formulation by controlling its pH.<sup>3</sup> Interestingly, addition of cetyl trimethyl ammonium bromide (CTAB) leads to photoluminescence quenching and increases hole transport in PEDOT:PSS. The film conductivity increases from 1.70 μS/cm to 2.25 μS/cm; due to a reorganization in its polymer's band structure resulting in a superior valence band matching with the MAPbI<sub>3</sub> layer.<sup>5</sup> DMSO and polyethylene oxide (PEO) serve as additives that improve the conductivity of PEDOT:PSS with a maximum value of 1000 S/cm.<sup>3,5</sup>

A solution-processed PEDOT film results in low substrate coverage stifling photocurrent and fill factor in planar PSCs. To overcome this limitation, in this study we address the acidity, low conductivity and low substrate coverage of solution-processed PEDOT:PSS by using a novel PSS-free PEDOT film synthesized via a Rust-based Vapor Phase Polymerization (RVPP) technique.<sup>12</sup> The RVPP technique is a facile and low-cost approach to fabricate highly conductive RVPP-PEDOT films with a conductivity of 1021 S/cm. This is the first investigation of its application as a HTL for MAPbBr<sub>3</sub> in PSCs.

In this work, we develop a deeper understanding of photophysical properties of the MAPbBr<sub>3</sub> film and interactions between RVPP-PEDOT/MAPbBr<sub>3</sub> interfaces by performing comprehensive spectroscopic studies of the RVPP-PEDOT/MAPbBr<sub>3</sub> and MAPbBr<sub>3</sub> devices. The MAPbBr<sub>3</sub> and RVPP-PEDOT/MAPbBr<sub>3</sub> nano-layers were deposited on fluorine doped tin oxide glass substrates and investigated with a set of static and time-resolved optical spectroscopies including state-state absorption, time-resolved photoluminescence and femtosecond time-resolved transient absorption. A battery of spectroscopic techniques was applied on a sample enabling

evaluation of opto-electronic MAPbBr<sub>3</sub> film properties such as charge carrier recombination rates under various excitation conditions, intensity dependent band filling effects, exciton binding energy and effective exciton reduced mass. Transient absorption spectroscopy was used to examine the FTO/RVPP-PEDOT/MAPbBr<sub>3</sub> device and to evaluate dynamics of hole extraction processes in RVPP-PEDOT/MAPbBr<sub>3</sub> interface and intrinsic charge recombination process within the MAPbBr<sub>3</sub> in the FTO/RVPP-PEDOT/MAPbBr<sub>3</sub> device.

## Materials and Methods

### *RVPP-PEDOT Film Preparation*

Fluorine-doped Tin Oxide (FTO) glass substrates (TEC™ 7) were purchased from MSE Supplies LLC, USA. The RVPP-PEDOT film was produced via Rust-based Vapor Phase Polymerization<sup>10, 11</sup> schematically depicted in Figure S1. First, the FTO glass substrates were washed subsequently with acetone and isopropyl alcohol in ultrasonic bath for 20 minutes, each. Then, to remove remaining organic impurities, the substrates were treated under UV-ozone for 30 minutes. Briefly, in subsequent step, a solid-oxidant precursor, 20-nm thick Fe<sub>2</sub>O<sub>3</sub>, was sputtered over the FTO via physical vapor deposition (Kurt J. Lesker PVD 75 RF and DC). A glass reactor was loaded with the Fe<sub>2</sub>O<sub>3</sub>-coated FTO, 40 μL of HCl, and 200 μL of a 0.67M EDOT solution in chlorobenzene, then sealed and heated in an oven at 140 °C for 1.5 h. The samples were purified via 6M HCl overnight to remove iron impurities. The sputtered α-Fe<sub>2</sub>O<sub>3</sub> was used as a ferric ion-containing solid-state oxidant-precursor to induce dissolution, liberation of ferric ions, and Fe<sup>3+</sup> hydrolysis with concomitant oxidative radical polymerization. The RVPP-PEDOT film was used as a hole transport layer (HTL).

### *Perovskite Film Deposition*

The MAPbBr<sub>3</sub> perovskite films were prepared using two step spin coating deposition technique. First, 1M PbBr<sub>2</sub> solution was prepared in N,N- dimethylformamide, heated up to 60 °C and continuously stirred for 30 min. Then, it was deposited on top of the RVPP-PEDOT layer by spin coating for 20 s at 5000 rpm and dried in two steps (50 °C and 100 °C) for 3 min and 5 min, respectively. To form the MAPbBr<sub>3</sub> perovskite, the MABr solution, prepared in anhydrous isopropanol (10 mg/mL) solution, was introduced to the PbBr<sub>2</sub> film through spin-coating at 0 rpm for 80 s and 4000 rpm for 20 s. For full perovskite conversion, the MABr deposition was repeated two times and at the end washed with IPA to remove excess amount of MABr followed by drying at 100 °C for 5 min. The whole deposition process and the solution preparation was performed under ambient conditions at relative humidity of 50%.

#### *Film surface and thickness analysis*

Thickness of RVPP-PEDOT and MAPbBr<sub>3</sub> perovskite films were analyzed with KLA Tencor D-100 series profilometer measuring 2D surface topography by using a stylus in close contact with the film surface. Quality of surface of RVPP-PEDOT film was evaluated by scanning electron micrographs with a JEOL 7001LVF Field-Emission Scanning Electron Microscope.

#### *Ultraviolet photo-electron spectroscopy*

Ultraviolet photo-electron spectroscopy (UPS) was carried out to identify the valence band (VB) maximum, conduction band (CB) minimum and bandgap ( $E_g$ ) of the RVPP-PEDOT deposited on silicon substrate using physical Electronics 5000 VersaProbe II Scanning ESCA Microprobe equipped with using He I (21.22 eV) and He II (40.8 eV) ultraviolet sources to provide information on the valence band of materials.

#### *Static and time-resolved optical spectroscopies*

All optical spectroscopic measurements were performed in dark at room temperature, in an air with humidity of ~40% on the samples prepared at the same day. Steady-state absorption spectra were measured using a Shimadzu 1800 UV-VIS spectrophotometer. From three samples prepared within single process the film with the best visual appearance of the surface and steady-state absorption spectrum was selected for further studies.

Time-resolved photoluminescence imaging (TRPL) was performed using Hamamatsu universal streak camera imaging system (Hamamatsu Corporation, Japan) employing the N51716-04 streak tube and Bruker A6365-01 spectrograph. The imaging setup was coupled to an ultrafast laser system described in detail previously.<sup>12</sup> The repetition rate of the exciting laser was set to 4 MHz (~250 ns between subsequent excitation). The excitation was set to 515 nm, the beam was depolarized using achromatic depolarizer (DPU25, Thorlabs) and focused on the sample in a circular spot of ~1 mm diameter. The excitation beam power was 100  $\mu\text{W}$ , corresponding to pump fluence of  $\sim 10^{10}$  photons  $\text{cm}^{-2}$ . Emission was measured at a right angle to the excitation beam with a 530 nm long-pass filter placed at the entrance slit of the spectrograph.

Transient absorption (TA) experiments were carried out using Helios-EOS, a tandem femtosecond/nanosecond time-resolved pump-probe absorption spectrometer (Ultrafast Systems) coupled to a Spectra-Physics femtosecond laser system described in detail previously.<sup>12</sup> The samples were excited at 480 nm. The energy of the excitation beam was adjusted between 0.002  $\mu\text{J}$  and 0.5  $\mu\text{J}$ , depending on scope of the study, corresponding to  $6.2 \times 10^{11} - 1.5 \times 10^{14}$  photons  $\text{cm}^{-2}$  (frequency excitation beam was set to 1 kHz, ~1 mm size excitation spot).

#### *Data analysis and fitting methods*

Group velocity dispersion present in the TA recorded in Helios was corrected using Surface Explorer 4 (Ultrafast Systems). Global fitting of selected TRPL and TA datasets was performed

using CarpetView (Light Conversion). Depending on kinetic model the fitting procedure gives amplitude spectra that in case of fitting of TA datasets with the simplest model assuming simultaneous photo-generation and independent parallel decay of spectroscopic species are commonly called DADS – decay associated difference spectra and relation between  $\Delta A(t, \lambda)$  and DADS is described by equation:

$$\Delta A(t, \lambda) = \sum_{i=1}^n C_i(t) DADS_i(\lambda) \quad (1)$$

where  $C_i(t)$ , is time-dependent concentration of  $i^{th}$  DADS expressed as  $C_i(t) = \exp(-k_i t) \times IRF(t)$  where IRF is instrument response function. By analogy if this fitting method is used to fit TRPL datasets, time and wavelength dependence of photoluminescence (PL) can be described according to equation:

$$PL(t, \lambda) = C_i(t) PLADS_i(\lambda) \quad (2)$$

where PLADS we define as photoluminescence associated decay spectra to differentiate them from DADS typically reserved for fitting of transient absorption. This fitting method was used to model TRPL decay image of the MAPbBr<sub>3</sub> film upon assumption that PL dynamics represent first order decay. For fitting of TA of RVPP-PEDOT/MAPbBr<sub>3</sub>, a more complex, so-called target analysis was applied.<sup>13</sup> That assumes that hypothetical pathways of excitation decay, or more adequately here, pathways of associated recombination of charge carriers are known. Fitting results of TA data according to predictive kinetic models are typically called SADS – species associated difference spectra and are associated with  $\Delta A(t, \lambda)$  via formula as presented in equation 1 in which DADS are replaced by SADS. However  $C_i(t)$  represents complex matrix that ensembles various kinetic interactions between individual SADS embedded in the fitting model.<sup>13</sup> The IRF was assumed to have a Gaussian-like shape with the full width at half maximum (FWHM) set to ~200

fs for Helios and 0.6 ns for streak camera setup (TRPL). Single wavelength fits and all plots were done in Origin 2020 (OriginLab Corp.).

## Results and discussion

### *MAPbBr<sub>3</sub> and RVPP-PEDOT VB/CB bands alignment, quality of RVPP-PEDOT film*

Building operational PEDOT/MAPbBr<sub>3</sub> device requires adequate alignment of VB and CB of both materials that will allow hole transfer from the perovskite to the polymer. Therefore first, UPS measurements were carried out to identify the VB maximum, CB minimum and Fermi level of the RVPP-PEDOT and how these correspond to their counterparts for the MAPbBr<sub>3</sub> perovskite film. Results are summarized in Figure 1.

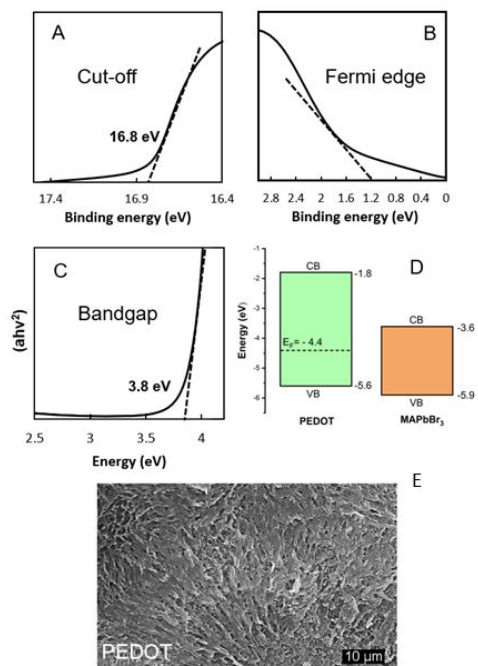
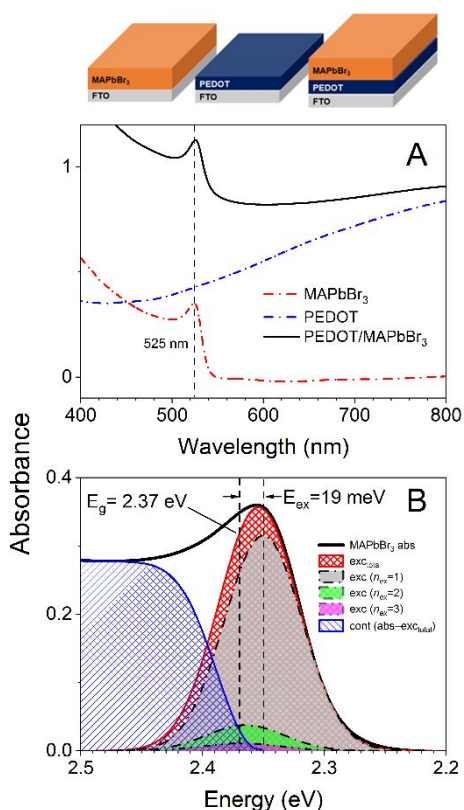


**Figure 1:** Electronic properties and surface quality of the RVPP-PEDOT film: (A) The cut-off energy ( $E_{\text{cut-off}}$ ) region; (B) Fermi edge ( $E_{\text{F-edge}}$ ) region; (C) Tauc plot obtained from the UPS spectra of the RVPP-PEDOT film on the FTO substrate; (D) Energy alignment of the RVPP-PEDOT and MAPbBr<sub>3</sub> perovskite layer; (E) Scanning electron micrographs (SEM) of the RVPP-PEDOT film deposited on FTO.

Fermi level ( $E_{\text{F}}$ ) of -4.4 eV was estimated from expression  $E_{\text{F}} = E_{\text{cut-off}} - 21.2$  eV (He 1 $\alpha$  emission line) with  $E_{\text{cut-off}}$  of 16.8 eV (Figure 1A) and  $E_{\text{VB}}$  is determined to be -5.6 eV from the Fermi edge shown in Figure 1B ( $E_{\text{VB}} = E_{\text{F}} - \text{edge} = -5.6$  eV). The RVPP-PEDOT bandgap was determined using the Tauc plot, which gives 3.8 eV (Figure 1C). Considering MAPbBr<sub>3</sub> VB of -5.9 eV and

CB of -3.6 eV, schematic band alignment for RVPP-PEDOT/MAPbBr<sub>3</sub> is presented in Figure 1D. It demonstrates that slightly lower  $E_{VB}$  energy (in absolute value) of the RVPP-PEDOT should facilitate hole transfer from the perovskite. On the other hand, significantly higher  $E_{CB}$  of the RVPP-PEDOT with respect to MAPbBr<sub>3</sub> can block the electron transfer from the perovskite to the RVPP-PEDOT which should be beneficial in reducing interfacial recombination. On the other hand, it is also important to have a RVPP-PEDOT film with few structural defects and uniformly coated FTO support preventing undesirable direct injection of photogenerated carriers from the perovskite layer into FTO substrate. The homogeneous morphology of our RVPP-PEDOT film is shown in the scanning electron micrograph in Figure 1E demonstrating complete coverage of the FTO substrate.

### Steady-state absorption of layers



Steady-state absorption spectra of the samples investigated in this work are presented in Figure 2, along with sketches of studied architectures. Figure 2A shows raw absorption spectra of three thin films deposited on the FTO support: 538-nm thick MAPbBr<sub>3</sub> perovskite (Figure S2), ~100-nm RVPP-PEDOT and combined RVPP-PEDOT/MAPbBr<sub>3</sub>.

**Figure 2.** Steady-state absorption spectra of thin film samples. (A) Absorption spectra of studied films, (B) Spectral reconstruction of the absorption spectrum of the MAPbBr<sub>3</sub> film in the range of the bandgap edge into contributions from excitonic ( $exc_{total}$ ) and continuum (cont) states. The energy gap of MAPbBr<sub>3</sub> ( $E_g$ ) obtained from the fitting is 2.37 eV (523 nm). The schematic representations of studied architectures are provided on the top of the figure. For more details refer to main text.

A baseline correction was done on the FTO glass plate, and for simplicity it will be omitted further in the text unless it will be necessary to mention. A basic comparison shows that the absorption spectrum of the MAPbBr<sub>3</sub> layer is minimally affected in the dual-layer film with respect to the perovskite-only layer. However, a marginal shift of the bandgap absorption by 1 nm to longer wavelengths is noticeable. Generally the band shape and rise of absorption of band-edge are comparable to their counterparts for the MAPbBr<sub>3</sub> film of a comparable thickness<sup>14</sup> or single MAPbBr<sub>3</sub> crystals.<sup>15, 16</sup>

It is evident that absorption band of the MAPbBr<sub>3</sub> film consists of two components, a prominent near-edge sharp band associated with electronic transitions to a series of excitonic states (electronic states of Coulombically bound electron-hole pairs) with maximum at ~525 nm and absorption to continuum states in the conduction band. Separation of both contributions may be achieved by applying Elliott's formula.<sup>17</sup> There are several versions of the expression available in literature sources<sup>16-20</sup> and for the modelling purpose the following form was adapted:<sup>19</sup>

$$Abs(E) = A E^{-1} \left( \frac{3}{E_{ex}^2} \sum_{n_{ex}}^{\infty} \frac{4\pi}{n_{ex}^3} \delta \left( E - E_g + \frac{E_{ex}}{n_{ex}^2} \right) + \frac{2\pi \sqrt{\frac{E_{ex}}{E - E_g}}}{1 - \exp \left( -2 \sqrt{\frac{E_{ex}}{E - E_g}} \right)} B \cdot \begin{cases} \sqrt{E - E_g}; & \text{if } E > E_g \\ 0; & \text{if } E < E_g \end{cases} \right) \quad (3)$$

where  $E$  is energy,  $A$  and  $B$  are constants,  $E_{ex}$  is exciton (electron-hole) binding energy,  $n_{ex}$  is positive integer associated with an order of the exciton electronic states,  $E_g$  is the energy gap between perovskite valence and conduction bands and  $\delta$  is a Dirac delta function. The first term describes contribution from series of bound excitonic states with energies  $-E_{ex}/n_{ex}^2$  below bandgap of energy  $E_g$ , the second part is associated with transitions to continuum states in the conduction band. The equation shows that strength of absorption of the subsequent excitonic lines precipitates very rapidly because intensity of the spectral line is proportional to  $1/n_{ex}^3$ . It greatly simplifies calculations and allows adequately simulate the experimental excitonic absorption spectrum with

only few initial lines. Results of the modelling with this approach are provided in Figure 2B. It was assumed that first three excitonic lines were sufficient for a satisfactory model ( $n_{ex} = 1, 2, 3$ ). In addition, for modelling of realistic room temperature spectrum  $\delta\left(E - E_g + \frac{E_{ex}}{n_{ex}^2}\right)$  functions were replaced with Gaussians having same arguments and linewidths of 64 meV. Figure 2B shows three first excitonic transitions (exc  $n_{ex} = 1, 2, 3$ ) and total excitonic band (exc<sub>total</sub>) obtained from their sum. As demonstrated, the modelled total excitonic band matches to the low energy tail of the experimental absorption spectrum. The fitting protocol returned  $E_g$  value of 2.37 eV and its position is marked on the graph with a dash line. The binding energy of electron-hole exciton in this MAPbBr<sub>3</sub> perovskite film was calculated as 19 meV. The absorption of the continuum states was simply obtained by subtracting the modelled excitonic band from the overall absorption spectrum of the perovskite film and this spectral component was not further evaluated. It is worth to note that binding energy of electron-hole exciton in perovskites was previously extensively experimentally studied as described below. Interestingly, for most common perovskite materials like MAPbI<sub>3</sub> and MAPbBr<sub>3</sub> there is no consensus on its value. For the former one few research groups determined it in low 2-8 meV range<sup>19, 21-23</sup> while others obtained much larger values of 24 meV<sup>24</sup>, 29 meV<sup>25</sup> or even 41.5 meV.<sup>16</sup> For perovskite type studied here, MAPbBr<sub>3</sub>,  $E_{ex}$  was reported at ~20 meV<sup>18</sup>, 21 meV<sup>26</sup>, 42 meV<sup>24</sup>, 60 meV<sup>25</sup> or even as high as 150 meV.<sup>27</sup> These are only values obtained from application of Elliot's formula to perovskite absorption spectrum, but these energetic ranges widen even further if results from other methods are included. For more details on this subject, we refer to recent reviews.<sup>28, 29</sup> Those large disagreements in  $E_{ex}$  value may origin from differences in assumptions done in empirical formulas of Elliot's equation used for fitting purposes but also from possible over-parametrization that may give non-unique fitting results. Nevertheless,  $E_{ex} = 19$  meV obtained here appears to fit into the expected energetic range.

Note that room temperature (293 K) corresponds to thermal energy of 25 meV therefore excited excitons are able to dissociate electrons to the conduction band.

### *Time-resolved photoluminescence*

Time-resolved photoluminescence (TRPL) results of the MAPbBr<sub>3</sub> film are shown in Figure 3. Figure 3A shows 2D pseudo-color TRPL profile obtained after excitation at 515 nm. The profile consists of a single emissive band with maximum at 540 nm that decays for a several nanoseconds. Figure 3B demonstrates expected steady-state PL spectrum that was obtained by integrating all TRPL spectra recorded within time domain of the profile. In addition, this spectrum was corrected for the transmittance spectrum of 530-nm long pass filter which was placed at the spectrograph slit to minimize leak of the excitation light and associated scattering effects.

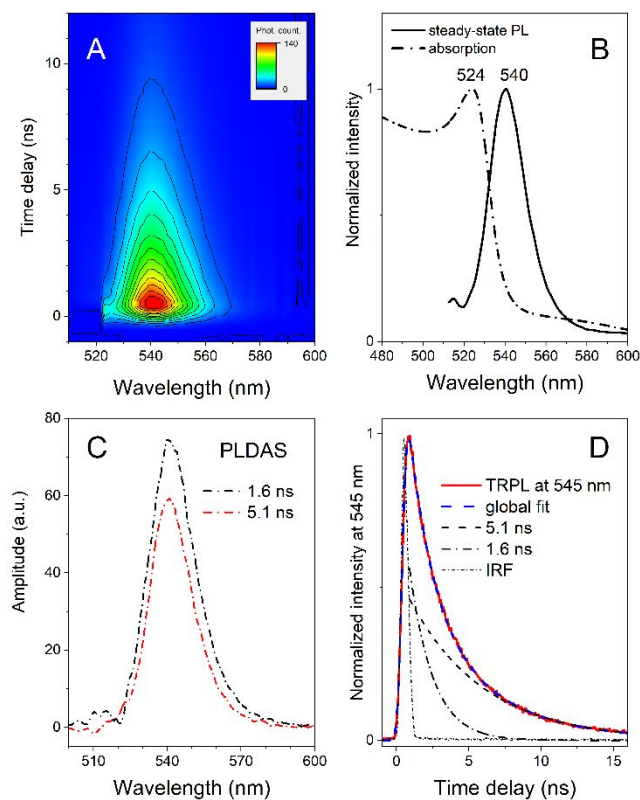


**Figure 3.** Time-resolved photoluminescence (TRPL) of 538-nm MAPbBr<sub>3</sub> film deposited on the FTO/glass support. (A) Pseudo-color 2D profile of PL decay recorded upon excitation at 515 nm, (B) Expected steady-state PL of the perovskite film obtained by integration of all TRPL spectra. The spectrum given in the graph was corrected for transmittance profile of 530 nm long-pass filter placed at the spectrograph entrance slit to minimize scattering effects, (C) PLDAS – PL Decay Associated Spectra - results of global fitting of the profile dataset from panel (A) with two non-interacting exponentially decaying components, (D) exemplary PL decay trace extracted from the decay profile accompanied by global fit, instrument response function (IRF) and contributions from two kinetic components (1.6 ns and 5.1 ns) obtained from global fitting.

Absorption spectrum of the perovskite film, added for reference, indicates that PL maximum is bathochromically shifted by 16 nm in respect to maximum of the excitonic band in the absorption spectrum. Radiative transition from conduction to valence band of perovskites is associated with band-to-band recombination of photogenerated carriers and its kinetics should be primarily represented by second order decay associated with bimolecular recombination.<sup>28</sup> However, generally the recombination dynamic of the photogenerated carriers is more complex and time evolution of charge carrier density  $n$  (/cm<sup>3</sup>) formed after photoexcitation is typically described by following equation:<sup>30</sup>

$$\frac{dn}{dt} = - (k_{SHR} + k_{surf})n - k_{bm}np - k_{Aug}n^3 \quad (3)$$

The  $(k_{SHR} + k_{surf})n$  term is the Shockley-Hall-Read (SHR) and surface assisted recombination via phonon-assisted nonradiative processes.<sup>28</sup> The  $k_{bm}np$  term corresponds to a bimolecular recombination of photoexcited electrons and holes ( $p$ ) and is considered an intrinsic radiative recombination that is related to the inverse of light absorption.<sup>19</sup> The term  $k_{Aug}n^3$  describes the processes of Auger recombination involving a nonradiative three-body process stemming from the recombination of an electron with a hole; this process transfers energy and momentum to another electron or hole.<sup>31</sup> Therefore, regardless of the spectroscopic method used for monitoring recombination of photogenerated charge carriers, e.g. time-resolved emission or absorption, in principle the recombination dynamics may be very complex with a non-trivial solution of  $n(t)$ . However, as demonstrated in the Equation 3, higher order recombination processes (bimolecular and Auger) are extremely sensitive for charge carrier concentration and would completely dominate recombination process if the density of photogenerated charge carriers is sufficiently elevated. These characteristics allowed to amplify or mitigate higher order recombination

processes and estimate ranges of carrier concentration for which a specific recombination process would dominate. In general, the SHR and surface assisted recombination is dominant if initial carrier density ( $n_0$ ) is  $<10^{15} \text{ cm}^{-3}$ , bimolecular recombination is a primary process for  $n_0$  between  $10^{15} \text{ cm}^{-3}$  and  $10^{18} \text{ cm}^{-3}$  and Auger recombination overwhelms recombination for  $n_0 > 10^{18} \text{ cm}^{-3}$ .<sup>28, 32, 33</sup>

The initial carrier density generated in the perovskite film in TRPL experiments was determined as described here. One can find that in literature a simple formula  $n_0 = \alpha I_{exc}$  (where  $\alpha$  is absorption coefficient of the film at excitation wavelength and  $I_{exc}$  is excitation light fluence) is used.<sup>33</sup> However, this formula is a simplification of more general equation for carrier generation rate  $n_0 = \alpha I_{exc} e^{-\alpha x}$ , where  $x$  corresponds to the film thickness. Therefore, simplified formula assumes zero-thickness perovskite layer that is not a case here. As seen from the equation above  $n_0$  will vary with dept of diffusion of excitation light into the film. Consequently, a more reasonable mean  $\langle n_0 \rangle$  was calculated:  $\langle n_0 \rangle = \alpha \langle I_{exc} \rangle$ . For that purpose, first the film  $\alpha(\lambda)$  was determined (Figure S3) and then  $\langle I_{exc} \rangle$  (Figure S4). Based on those results following formula was obtained:  $\langle n_0 \rangle = 0.7 \alpha I_0$  where  $I_0$  corresponds to photon flux at the surface of the sample. Considering  $\alpha_{515nm} = 1.4 \times 10^4 \text{ cm}^{-2}$  (Figure S3C) and  $I_0 = 10^{10} \text{ photons cm}^{-2}$  (Materials and methods)  $\langle n_0 \rangle = 1 \times 10^{14} \text{ cm}^{-3}$ . Such carrier density suggests that recombination process will be primarily associated with a monomolecular recombination and should be clearly distinguished from other processes in PL dynamics due to first order decay character. It is worth noting that TRPL does not exclusively distinguishes the radiative component in Equation 3 but its dynamics still represents overall temporal evolution of  $n(t)$  that only approximately reflects kinetic character of the most contributing process. Therefore, for  $\langle n_0 \rangle$  of  $\sim 10^{14} \text{ cm}^{-3}$  dynamics of PL decay from the beginning will rather follow first order decay associated with monomolecular recombination stemming

mostly from surface defects and traps. The rate order of the PL could be easily evaluated by taking inverse of PL intensity ( $I_{PL}$ ) or by plotting  $\ln(PL)$  as function of  $t$ . If PL evolves with the second order decay  $1/PL$  should reveal linear function  $t$  or if according to a first order,  $\ln(PL)$  will reveal linear character. These plots are given in Figure S5A,B and show that PL decay has rather exponential (most likely two exponentials) character. It is also apparent that increase of pump fluence would gradually fill all defects and traps and at specific fluence onset of the second order decay in the PL dynamics will reveal as conduction band will fill with free photoexcited carriers. This critical pump fluence could be used to determine the density of trapping sites in the perovskite film<sup>34</sup> though we have not investigated it.

Exponential-like character of PL decay allows to perform basic global fitting of the whole TRPL decay profile according to Equation 2 (refer to experimental section) as shown in Figure 3C; results show amplitude spectra labeled PLDAS (Photo-Luminescence Decay Associated Spectra). The global fitting demonstrated that upon applied excitation condition PL decays with two different time constants of 1.6 ns and 5.1 ns. Both PLDAS are similar in spectral shape and position but have slightly different amplitudes. Contribution of those spectro-kinetic components in the exemplary PL decay trace taken at 545 nm is given in Figure 3D. That decay trace is also accompanied by global fit and IRF curve used to convolute fit. The amplitude-weighted PL lifetime,  $\tau_{(aw)PL}$ , derived from abovementioned kinetic components is 3.2 ns. For comparison, the PL lifetime of comparable MAPbBr<sub>3</sub> film obtained by other group under similar experimental conditions was 51 ns.<sup>14</sup> Such substantial inconsistency in the PL temporal characteristics may occur from few sources. It is possible that PL dynamics has contribution from a second-order decay associated with bimolecular recombination though this possibility seems to be small due to excitation intensity applied in this study. In order to confirm or exclude it we fitted the kinetic

trace from Figure 3D with sum of first and second order decays. Results provided in Figure S5C show that the fitting does not converge with experimental curve meaning that the short-lived component has different origin. Another possibility that may explain multiexponential character of the PL decay and substantially faster dynamics compared to its peer from other study is that the film studied in this work is very homogenous with the semiconductor grains spanning entire width of the film. For such structures a very efficient vertical charge diffusion is expected with large values of diffusion coefficient ( $D$ ) and surface recombination velocity ( $S$ ). Mathematical models of semiconductor PL decay with diffusion component having large  $D$  and  $S$  demonstrated that the decay shortens multiple times and in addition may reveal multiexponential-like character, similarly as observed here.<sup>35</sup> Consequently, in order to obtain correct PL decay lifetime the experimental curve should be fitted with solution of equation 3 including charge diffusion component. However to avoid complex fitting equation with many variable parameters we alternatively applied fit with a stretched exponential decay that is sometimes used as simplification of that approach.<sup>36</sup> Successful application of this fitting method to the experimental PL decay trace is provided in Figure S5D. The fitting gave PL decay lifetime of 1.9 ns.

#### *Time-resolved absorption of MAPbBr<sub>3</sub> film*

Time-resolved absorption results of the MAPbBr<sub>3</sub> film taken within 5 ns after excitation with 100-fs laser pulse at 480 nm are shown in Figure 4. Figures 4A and B show pseudo-color profiles of TA recorded upon low (0.002  $\mu$ J) and high (0.5  $\mu$ J) excitation energy, respectively. The TA profiles consist prominent bleaching band with minimum at  $\sim$ 525 nm. It is also evident that excessive excitation strongly influences spectral features at early delay times. The most apparent is substantial spectral broadening of the bleaching band and appearance of the weak negative band at  $\sim$ 540 nm probably associated with the probe-stimulated PL. It is demonstrated in Figure 4C in

which series of TA spectra recorded at 3 ps for several excitation energies is plotted. The spectra were normalized to minimum for better comparability and clearly demonstrate that higher excitation energy leads to gradual increase of the bleaching band width and rise of stimulated PL. More insight on spectral appearance of TA spectra on excitation energy at various delay times are shown in Figure S4. Excitation intensity has also apparent effect on the TA dynamics. Figure 4D shows set of the TA traces recorded at the minimum of the bleaching band. The traces are normalized into their initial “plateau” that is reached after 3-5 ps from excitation moment and are plotted in semi-log time scale to better visualize differences within entire delay time scale. As demonstrated, recovery of the bleaching band substantially accelerates upon increase of the excitation energy (intensity).

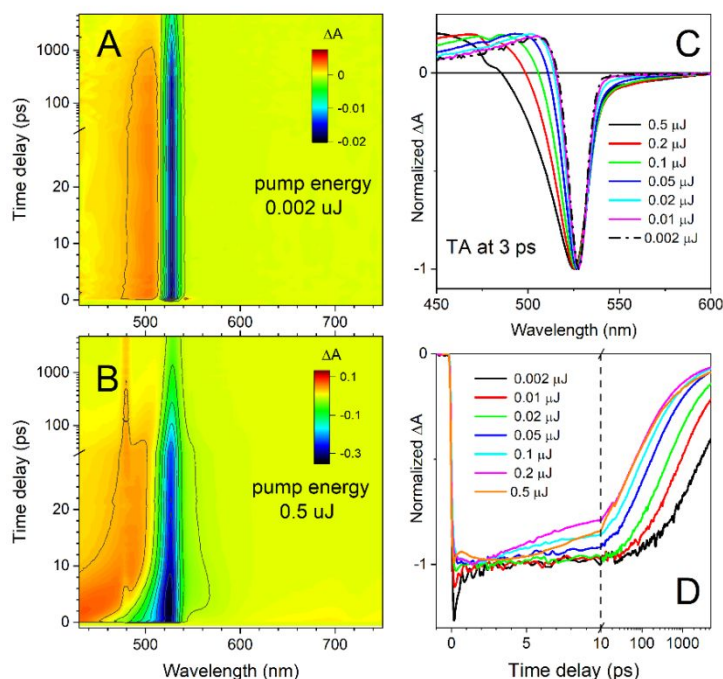


**Fig. 4.** Transient absorption results of 538-nm thick MAPbBr<sub>3</sub> film upon excitation at 480 nm with various excitation energies (intensities). (A, B) Pseudo-color profiles of TA obtained for the lowest (0.002 μJ) and the highest (0.5 μJ) excitation energies used in this study, respectively; (C) TA spectra taken at 3 ps after excitation with different energies. The spectra, for better comparability, are normalized at their minima; (D) TA dynamics at wavelengths corresponding to minimum of bleaching of band gap absorption (normalized to their initial plateaus, at 3-5 ps).

A subsequent Figure 5 shows correlation between pump energy with initial average density of generated carriers ( $n_0$ ) and optical response of the film denoted as “Bleach area” which corresponds to absolute area of bleaching band calculated after converting wavelength scale to linear wavenumber scale. The area was calculated at 1 ps after excitation, time delay at which the

bleach band reached its minimum (absolute maximum). It highlights that the strength of the TA signal (denoted as overall bleaching) does not have linear response to pump energy and saturation effects are noticeable. This property is well-known for many materials including perovskites<sup>32, 37</sup> and suggests that absorption coefficient of this perovskite film is intensity dependent. As marked on the figure, the initial carrier densities  $\langle n_0 \rangle$  generated with laser excitation spans broad range from  $10^{16}$  to  $10^{18}$   $\text{cm}^{-3}$ . Extend of the bleaching (BA) can be adequately approximated with function of initial charge carrier density  $n_0$  in the following form  $BA = \frac{a\langle n_0 \rangle}{b + \langle n_0 \rangle^c}$  where  $a$ ,  $b$ ,  $c$  are fit parameters.<sup>31, 33</sup> The fit along with fitting parameters is also presented in Figure 5.

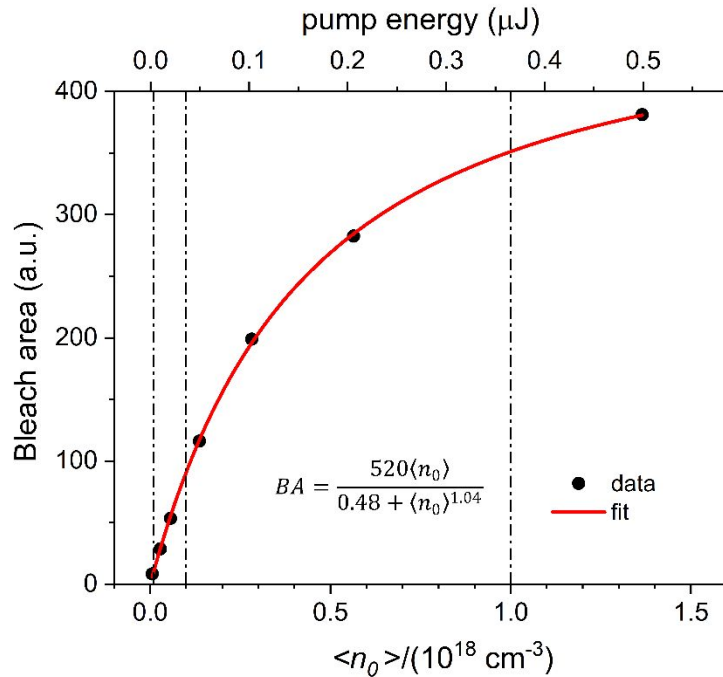


**Figure 5.** Saturation curve of bleaching band of the MAPbBr<sub>3</sub> film. Pump energy ( $\mu\text{J}$ ) was converted to initial charge carrier density  $\langle n_0 \rangle$ . The experimental points of bleach area were fitted with expression as provided in the figure. Reference vertical lines correspond to  $\langle n_0 \rangle = 1 \times 10^{16}$ ,  $10^{17}$  and  $10^{18}$   $\text{cm}^{-3}$ .

Typically, a very simple method of plotting inverse of the  $\Delta A$  as function of the delay time  $t$  is used to determine kinetic order of the TA traces. For a truly bimolecular recombination (second order decay) this expression will have a linear dependency from  $t$  and that allows to fit the trace simply by applying second-order decay integration law. However, one can see that it is a common practice to plot numerous dynamic traces from different excitation intensities on the same

graph, procedure that artificially flattens traces from lower excitation intensities and may give a false perception of a near perfect linearity across a broad range of excitation intensities. This is very likely not the case as other types of recombination always has some contributions in the overall process and their weights will vary greatly with excitation intensity and charge carrier density  $n(t)$  evolving over time delay. To evaluate if recombination process recorded in TA traces (within 5-ns time window) follows a bimolecular recombination, we adopted formula occasionally used to confirm second order rate character of chemical reactions<sup>38</sup>

$$\frac{t}{1 - \frac{n(t)}{\langle n_0 \rangle}} = \frac{1}{k\langle n_0 \rangle} + \frac{N}{2}t \quad (5)$$

where  $k$  is recombination rate constant,  $\langle n_0 \rangle$  is the mean initial charge carrier density as defined earlier and  $n(t)$  is charge carrier density over delay time  $t$  (TA kinetic trace) and  $N$  is recombination rate order. Results of this analysis for TA kinetics from Figure 4D are provided in Figure 6. Analysis clearly indicates that recombination process, represented in TA as recovery of transient bleaching band does not have the same kinetic character across the range of excitation intensities used in the study. For comparison, a hypothetical kinetic trace having a second order decay character (black, dash line), was arbitrarily placed to complement experimental data.

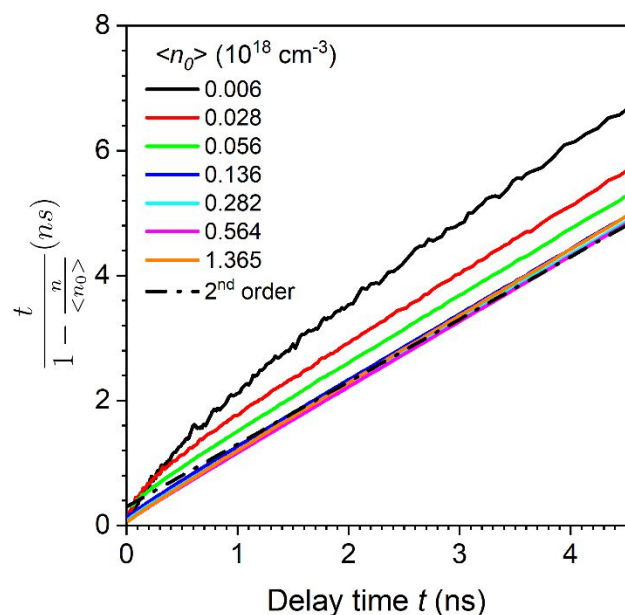


**Figure 6.** Evaluation of decay rate order of TA kinetics recorded at various excitation intensities. Dashed black line is a hypothetical 2<sup>nd</sup> order decay arbitrarily placed on the graph for the best match. Plot suggests that overall recombination process is dominated by bimolecular recombination for initial charge carrier intensities  $\langle n_0 \rangle \geq 1.36 \times 10^{17} \text{ cm}^{-3}$ . For lower intensities, the kinetics are most likely a combination of first and second order decays without a simple linear representation.

From performing linear fits for all those traces (not shown), the TA traces that are kinetically the closest to the second order decay are those for  $\langle n_0 \rangle = 0.282$  and  $0.564 \times 10^{18} \text{ cm}^{-3}$  with slopes corresponding to  $N = 2.12$  (vs  $N = 2$  for a hypothetical second order decay, Equation 5). From intercepts of those two most representative decays an average bimolecular recombination rate was calculated and  $k_{bm} \approx 2.6 \times 10^{-10} \text{ cm}^3 \text{ s}^{-1}$ . As demonstrated below, data show that  $k_{bm}$  value obtained in this work falls within expected range. In comparison, for MAPbI<sub>3</sub> perovskite, Manser et al.<sup>33</sup> obtained  $k_{bm} = 2.3 \times 10^{-9} \text{ cm}^3 \text{ s}^{-1}$  for ~600-nm thick film, Piatkowski et al.<sup>32</sup> reported  $k_{bm}$  of  $25.1 \times 10^{-9} \text{ cm}^3 \text{ s}^{-1}$  for 200-nm thick film while Wehrenfennig et al.<sup>39</sup> for ~400-nm thick film obtained  $k_{bm} = 9.2 \times 10^{-9} \text{ cm}^3 \text{ s}^{-1}$ . For MAPbBr<sub>3</sub> film  $k_{bm} = 1.5 \times 10^{-10} \text{ cm}^3 \text{ s}^{-1}$  was reported<sup>40</sup> closely comparable with our findings.

#### *Band filling effect*

Spectral broadening of the bleaching band upon increase of excitation intensity is clearly observed in TA spectra taken at various delay times (Figure S6) however is particularly noticeable in the early delay TA spectra (Figure 4C). The change of the bleaching band was explained by dynamic Burstein-Moss (BM) shift.<sup>41, 42</sup> Pump with higher fluence promotes more electrons to conduction band and accordingly larger population of holes is accumulated in valence band. These species immediately energetically relax to occupy energy sites near both band edges. As results demonstrate, these energetic sites in both bands are excluded from consecutive excitation by broadband probe pulse until charge carriers recombine. Consequently, the bleaching band (that corresponds to the bandgap edge) is initially very broad due to filling effect, but it narrows as delay time elapses. The dynamic increase in bandgap energy can be calculated as increase of the width of the bleaching band measured at time delay at which intra-band energetic relaxation of photoexcited charge carriers has completed (note that 480 nm excitation is 0.2 eV above

bandgap).<sup>32, 33</sup> For that purpose TA spectra recorded at 2 ps after excitation pulse were chosen. According to BM model the bandgap increase relates to charge carrier density  $n$  via following expression

$$\Delta E_g^{BM} = \frac{\hbar^2}{2\mu} (3\pi^2 n)^{\frac{2}{3}} \quad (6)$$

where  $\Delta E_g^{BM}$  is change in the bandgap energy due to Burstein-Moss (BM) band filling effect,  $\hbar$  is reduced Planck constant,  $\mu$  is reduced effective mass of photoexcited electron-hole pair defined as  $\mu = (m_e^{*-1} + m_h^{*-1})^{-1}$  where  $m_e^*$  and  $m_h^*$  are effective masses of electron and hole, denominated in rest mass of electron ( $m_0$ ). Experimental confirmation of Equation 6 is provided in Figure 7.

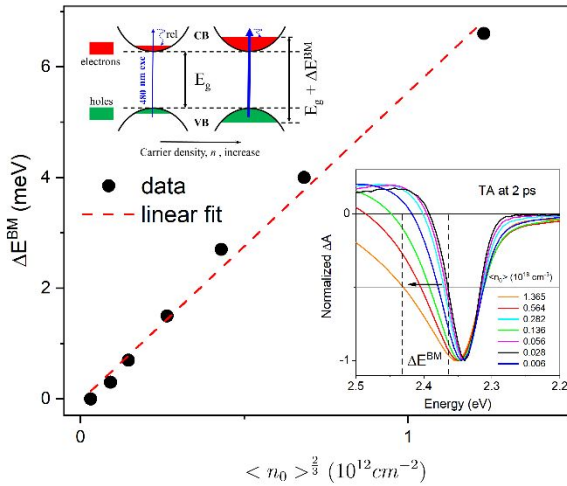


**Figure 7:** Transient increase of the intrinsic bandgap due to band filling effect according to the Burstein-Moss (BM) model.<sup>41, 42</sup> The bandgap increase ( $\Delta E^{BM}$ ) is calculated as increase in FWHM of the bleaching band resulting from higher initial charge carrier density ( $n_0$ ) (lower insert). The  $\Delta E^{BM}$  was calculated from TA spectra taken at 2 ps after excitation. Schematic representation of the BM effect is shown in upper insert. VB, CB – valence and conduction band, respectively, exc – excitation.  $E_g$  – intrinsic energy gap, rel – energetic relaxation within CB. Thicker blue arrow represents higher excitation intensity.

According to Equation 6,  $\Delta E^{BM}$  should be a linear function of  $n^{2/3}$ . It was assumed that  $n$  at 2 ps after excitation essentially corresponds to  $\langle n_0 \rangle$  and  $\Delta E^{BM}$  was plotted as function of  $\langle n_0 \rangle^{2/3}$ . Linear fit of data points mimics trend in data point and confirms validity of explanation of the spectral broadening. Value of the slope of the linear fit (0.0558) was used to calculate reduced exciton mass which is:  $m_{eh}^* = 0.19 \times m_0$ . That estimate correlates well to previous valuations for either MAPbI<sub>3</sub> or MAPbBr<sub>3</sub> perovskites:  $0.1 \times m_0$ <sup>32, 43</sup>,  $0.15 \times m_0$ <sup>44</sup> or  $0.3 \times m_0$ <sup>33</sup>.

*Transient absorption of RVPP-PEDOT*

For proper TA analysis, it should be noted that due to a much smaller thicknesses of the MAPbBr<sub>3</sub> and RVPP-PEDOT films compared to the spatial overlap of pump and probe beams, it is impossible to preferentially excite MAPbBr<sub>3</sub> layer in the FTO/RVPP-PEDOT/MAPbBr<sub>3</sub> device without simultaneous excitation of the polymer film. Consequently, in order to correctly understand all spectral features of the TA spectra of FTO/RVPP-PEDOT/MAPbBr<sub>3</sub> architecture it is necessary to determine if excitation of the polymer film at wavelength used to excite perovskite (480 nm) also generates TA signal. To clarify this issue, TA studies of the 100-nm thick RVPP-PEDOT polymer film (Figure S7) deposited on FTO support were performed. The TA results are provided in Figure S8. In an ideal scenario the RVPP-PEDOT used in this study should not reveal any TA signal upon excitation at this wavelength. It is because the chemical treatment applied during polymerization gives oxidized *p*-doped PEDOT film with steady-state absorption consisting mixture of polarons and bipolarons absorbing exclusively in the infrared spectral range.<sup>45-48</sup> This is clearly seen in absorption spectrum of the RVPP-PEDOT (Figure 2A) – film absorption substantially increases at longer wavelengths. A non-zero absorbance below 500 nm is most likely associated with light scattering of the film that cannot be corrected in a standard setup of the spectrophotometer used in this study but from this perspective absorption spectrum of the PEDOT film does diverge from those measured by other research groups.<sup>45</sup> Figure S8 demonstrates that the RVPP-PEDOT film reveals TA signal in form of a negative band across whole spectral range and its strength is linearly dependent from excitation intensity. Considering mismatch with the RVPP-PEDOT absorption it suggests that the recorded TA features are likely artifacts, probably associated with processes like e.g., excitation induced thermal expansion and

relaxation of the film that may transiently affect its physical properties like refractive index, scattering efficiency, etc.

### *Transient absorption of RVPP-PEDOT/MAPbBr<sub>3</sub>*

Finally, transient absorption spectroscopy was applied to study hole extraction process from the photoexcited MAPbBr<sub>3</sub> film in the FTO/ RVPP-PEDOT/MAPbBr<sub>3</sub> architecture. It is worth noting that femtosecond or nanosecond time-resolved absorption was used to investigate hole extraction from MABPbI<sub>3</sub> perovskite interfacing various HTL-type conducting polymers as: poly(3,4-ethylenedioxythiophene)-poly(styrenesulfonate) (PEDOT:PSS)<sup>49, 50</sup>, poly(diketopyrrolopyrrole-terthiophene) (PDPP-3T)<sup>51</sup>, poly(triarylamine) (PTAA), poly(3-hexylthiophene-2,5-diyl (P3HT), and poly[2,6-(4,4-bis-(2-ethylhexyl)-4H-cyclopenta [2,1-b;3,4-b']dithiophene)-alt-4,7(2,1,3-benzothiadiazole)] (PCPDTBT).<sup>52</sup> Taken together these provide rather unclear picture of hole extraction mechanism, especially on time constants of the process appearing from fraction of picosecond<sup>50</sup> to few nanoseconds.<sup>51, 52</sup> Here we applied femtosecond time-resolved absorption on RVPP-PEDOT/MAPbBr<sub>3</sub> and compared the results with our investigations performed on the MAPbBr<sub>3</sub> film. Some previous studies of PEDOT:PSS/MABPbI<sub>3</sub> suggested sub-picosecond hole extraction<sup>50</sup> therefore primary focus was on early delay spectral features but subsequently also an overall charge recombination dynamics were analyzed in complementary TA signals of the RVPP-PEDOT/MAPbBr<sub>3</sub> and MAPbBr<sub>3</sub> films. The results are provided in Figure 8 and in Figure S9. Because it is anticipated that hole extraction occurs within couple of picoseconds after excitation of the perovskite<sup>50</sup> it should be very informative to compare TA spectra of MAPbBr<sub>3</sub> taken immediately after excitation with those at delay times at which hole extraction process is most probably completed. These spectra are given in Figure 8A and B. The

figures show TA spectra of MAPbBr<sub>3</sub> in the FTO/MAPbBr<sub>3</sub> architecture taken at 330 fs and 2.5 ps and comparable MAPbBr<sub>3</sub> TA spectra (440 fs and 2.5 ps) taken for the FTO/RVPP-PEDOT/MAPbBr<sub>3</sub>, both after excitation at 480 nm.

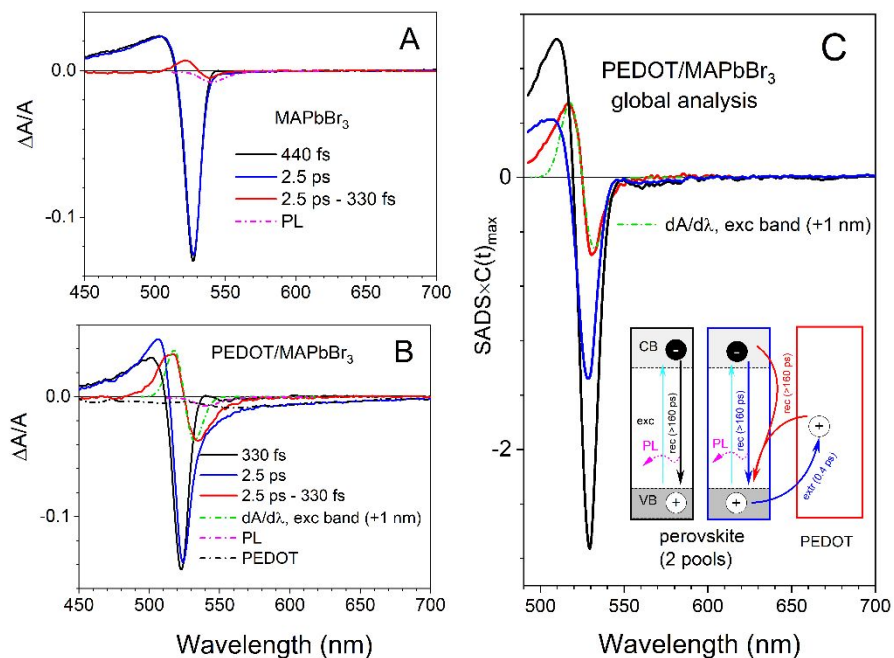


**Figure 8:** Comparison of initial TA spectra of the MAPbBr<sub>3</sub> and RVPP-PEDOT/MAPbBr<sub>3</sub> films under comparable excitation conditions and global analysis of TA data of RVPP-PEDOT/MAPbBr<sub>3</sub> collected within first 200 ps. (A) Raw TA spectra of MAPbBr<sub>3</sub> taken at 440 fs and 2.5 ps, difference between them and scaled PL spectrum for reference; (B) Complementary TA spectra of RVPP-PEDOT/MAPbBr<sub>3</sub>, difference, scaled PL spectrum and first derivative of excitonic band from MAPbBr<sub>3</sub> absorption spectrum; (C) Global analysis results of first 200-ps RVPP-PEDOT/MAPbBr<sub>3</sub> TA data according to kinetic scheme provided as insert. All SADS components were corrected for hypothetical contributions of stimulated PL and TA contribution from directly induced TA of RVPP-PEDOT. For more details refer to the main text.

It should be noted that to assure that primarily MAPbBr<sub>3</sub> interfacing RVPP-PEDOT layer is excited, the FTO/ RVPP-PEDOT/MAPbBr<sub>3</sub> device was excited through FTO/RVPP-PEDOT side. Consequently, nominally the same excitation energy (intensity) as used for PEDOT-free sample generates vastly different TA signal for PEDOT/MAPbBr<sub>3</sub> due to a substantial excitation light scattering in the polymer film (see Figure 2A). Therefore, excitation intensity was adjusted until it

generated  $\Delta A/A$  signals comparable with those obtained for MAPbBr<sub>3</sub> in the FTO/MAPbBr<sub>3</sub> device, as seen in Figure 8A and B. These  $\Delta A/A$  correspond to recombination kinetics of  $\langle n_0 \rangle = 0.028 \times 10^{18} \text{ cm}^{-3}$ . For reference, the scaled and inverted MAPbBr<sub>3</sub> PL spectrum is added (magenta). A small difference between TA spectra of MAPbBr<sub>3</sub> recorded at 330 fs and 2.5 ps (red line, 2.5 ps TA - 330 fs TA) is most likely associated with intra-band energetic equilibration of photoexcited carriers (positive part of difference spectrum) and rise of stimulated PL (negative part of difference spectrum). For RVPP-PEDOT/MAPbBr<sub>3</sub> sample, a comparable analysis reveals a very different picture. First, the TA spectrum recorded at 2.5 ps shows additional bleaching on the long wavelengths side of the main bleaching band that extends up to 700 nm. This additional signal resembles RVPP-PEDOT TA spectrum recorded upon the same excitation wavelength, provided as black dash-dot line. If 2.5-ps TA spectrum is corrected for its contribution and subsequently 330-fs TA spectrum is subtracted, resulting difference spectrum (red line) cannot be explained as its counterpart for MAPbBr<sub>3</sub> film because (i) spectrum position is different, (ii) signal magnitude is too large and (iii) the negative part mismatches with the spectrum of expected stimulated MAPbBr<sub>3</sub> PL (magenta). Interestingly, the difference spectrum (red line) can be very adequately mimicked by first derivative of absorption spectrum of the excitonic band obtained from the modeling of the bandedge absorption spectrum of MAPbBr<sub>3</sub> (Figure 2C) (the band was first shifted 1 nm to longer wavelengths to match its position in the FTO/RVPP-PEDOT/MAPbBr<sub>3</sub> architecture (Figure 2A)). Previously it was demonstrated that excitons in semiconductor nanocrystals have large polarizability,<sup>53</sup> property that to some extent should be carried by excitons in the semiconductor nano-layers like these studied here. Consequently an exciton, a Coulombically bound electron-hole pair, placed in an external electric field will show strong electrochromic response (Stark effect).<sup>53</sup> The Stark spectrum, a difference spectrum of absorption

spectra system/molecule in external electric field on and off is typically modeled with Liptay formula as a linear combination of the absorption spectrum and its first and second derivatives as follows<sup>54</sup>

$$\Delta A(\nu) = a_0 A + a_1 \frac{dA}{d\nu} + a_2 \frac{d^2 A}{d\nu^2} \quad (7)$$

where  $A$  is absorbance,  $\Delta A$  is change in absorbance,  $\nu$  is wavenumber [ $\nu$  ( $\text{cm}^{-1}$ ) =  $10^7/\text{nm}$ ]. The equation coefficients  $a_{0-2}$  are related to ( $a_0$ ) the field-induced change in the electronic transition moment and changes of ( $a_1$ ) polarizability and ( $a_2$ ) dipole moment of an excited state. It was shown that Stark spectrum of the semiconductor (CdSe) nanocrystallites can be explained by polarizable and delocalized nonpolar excited states. For this nanocrystallite, the Stark effect was associated with change in polarizability of exciton excited states and was adequately modeled by Liptay formula comprising only term with first derivative of the semiconductor absorption spectrum.<sup>55</sup> If we draw analogy here, additional signal present in the TA spectra of the RVPP-PEDOT/MAPbBr<sub>3</sub> could be associated with change in polarizability of exciton excited states due to small perturbation from external electric field. This electric field will be locally induced only in the RVPP-PEDOT/MAPbBr<sub>3</sub> interface upon spatial charge separation resulting from hole extraction to RVPP-PEDOT film. Therefore, dynamics of the rise of transient Stark spectrum in the TA data could be interpreted as time constant of buildup of the electric field and in principle should reveal dynamics of hole extraction process. The dynamics of that process was evaluated by applying global analysis on the entire RVPP-PEDOT/MAPbBr<sub>3</sub> TA dataset used to extract spectra shown in Figure 8B. Results are provided in Figure 8C and were obtained according to the kinetic scheme depicted schematically in the insert. Because the fitting algorithm is based on first order rates but the overall recombination process is more complex, only the initial 200-ps time span of the dataset

was used to make fitting process more reasonable. If anticipated fitting model closely resembles dynamics of real physical processes manifested in time evolution of the TA data, the fitting results (SADS) spectrally separate transient signals that are blended in raw TA spectra. The SADS are given in Figure 8C and in order to better visualize their relative ratio in the raw TA signal, all SADS were normalized to their maximal contributions in the raw signal by multiplication of SADS by amplitudes of their time-dependent concentrations  $C_{max}(t)$ . In addition, all SADS were also corrected for contributions from stimulated MAPbBr<sub>3</sub> PL and transient artifacts associated with direct excitation of the RVPP-PEDOT film. Results of global analysis could be interpreted as follows. The RVPP-PEDOT/MAPbBr<sub>3</sub> sample is not homogeneous in meaning that excitation at 480 nm generates two pools of photoexcited carrier populations, one that will intrinsically recombine within semiconductor (black arrow and SADS) and second that will be involved in PEDOT-assisted hole extraction process (blue arrows and SADS). Once MAPbBr<sub>3</sub>-to-RVPP-PEDOT charge separation occurs, due to holes extraction, local electric field on the MAPbBr<sub>3</sub>/RVPP-PEDOT interface formed due to spatially separated electrons and holes will induce Stark spectra by perturbing excited states of unexcited fraction of excitons located in the MAPbBr<sub>3</sub>/RVPP-PEDOT interfacial area within probe beam spot. Fitting demonstrated that holes extraction occurs with time constant of 0.4 ps immediately after excitation, being with agreement with previous sub-picosecond estimate for PEDOT:PSS used as HTL in MAPbI<sub>3</sub>-based architecture.<sup>50</sup> It should be noted that this time constant corresponds specifically to interfacial injection process and is typically called as interfacial injection rate and does not characterize overall charge transfer process that dynamically comprises charge diffusion within perovskite film and interfacial hole extraction. It is worth noting that there are more estimates of hole extraction constant for spiro-OMeTAD and MAPbI<sub>3</sub> interfaces however there is no consensus between results

as those vary from  $\sim 80$  fs to 8 ps.<sup>32, 52, 56, 57</sup> In this context 0.4 ps value obtained here falls within the range of expectations. Note that induced Stark spectrum would not diminish until spatially separated charges will recombine therefore its decay is entangled with recombination dynamics. It is also interesting to evaluate if efficient and ultrafast holes extraction from MAPbBr<sub>3</sub> affects the overall recombination process (transient bleach recovery dynamics). The TA dynamics recorded for both samples of comparable  $\langle n_0 \rangle$  or  $(\Delta A_{\max}/A)$  are shown in Figure S9A which demonstrates that for RVPP-PEDOT/MAPbBr<sub>3</sub> decay of comparable TA occurs much faster. It is tempting to interpret these changes as apparent quenching associated with hole extraction process that combined with charge diffusion process of charges within perovskite film leads to observed altered recombination dynamics. Proper kinetic modeling of that process (represented as recovery dynamics of transient bleach) would require more complex kinetic equation that includes quenching and diffusion terms as applied previously.<sup>57</sup> First, application of more complex model of recombination dynamics on the data should be justified. However simply analysis of rate order of the TA decay (bleach recovery) given in Figure S9B reveals that charge recombination can be perfectly described with second order decay within the time window of the measurement therefore it is clearly associated with bimolecular recombination and no additional processes need be included to adequately fit the recombination dynamics. It should be noted that previously, evolution of charge density with included diffusion and interfacial electron-transfer and charge recombination terms were globally applied for the set of TA dynamics collected under the same excitation condition for the perovskite/electron or hole extraction layer samples having varying semiconductor film thicknesses. We have not performed such studies (we measured single 540-nm thick perovskite film) and fact that TA dynamics is entirely dominated by bimolecular

recombination term could be just coincidental but unfortunately prevents further elaboration of overall charge transfer process.

## Conclusions

In this work we have studied the 538-nm film of organometal halide perovskite  $\text{MAPbBr}_3$  deposited on fluorine doped tin oxide glass and the architecture with the perovskite film covered with ~100-nm layer of polymeric hole transporting material (RVPP-PEDOT) for its possible application in photovoltaic solar cells. Investigations exclusively focused to define basic photophysical properties of perovskite material like bandgap and exciton binding energies, photoexcited charge carrier recombination dynamics and characterization of  $\text{MAPbBr}_3$ -to-RVPP-PEDOT hole extraction process. Studies were performed with application of steady-state absorption, time-resolved photoluminescence imaging and femtosecond time-resolved absorption at room temperature. Comparative spectro-temporal analysis of spectroscopic data of the FTO/ $\text{MAPbBr}_3$  and FTO/RVPP-PEDOT/ $\text{MAPbBr}_3$  architectures revealed very short time constant of holes extraction of 0.4 ps. As fast as possible hole extraction is very desirable as it guarantees efficient competition with intrinsic charge carrier recombination, process that dynamically could substantially vary, depending on light condition to which absorber (perovskite layer) is exposed to. A sub-picosecond  $\text{MAPbBr}_3$ -to-RVPP-PEDOT hole extraction time constant suggests that RVPP-PEDOT is potentially very good to serve as efficient hole extracting/transporting material for application in perovskite-based photovoltaic solar cells.

## Conflicts of interest

There are no conflicts to declare.

## Acknowledgments

D.N.M. acknowledges Center for Solar Energy and Energy Storage at McKelvey School of Engineering at Washington University in Saint Louis for financial support. M.K. and P.B. acknowledge the partial support from NSF DMR-1806147.

## References

1. <https://www.nrel.gov/pv/cell-efficiency.html>).
2. M. Kouhnavard, D. M. Niedzwiedzki and P. Biswas, *Int J Energ Res*, 2020, **44**, 11354-11371.
3. M. Yi, W. Jang and D. H. Wang, *Acs Sustain Chem Eng*, 2019, **7**, 8245-8254.
4. L. J. Hu, M. Li, K. Yang, Z. Xiong, B. Yang, M. Wang, X. S. Tang, Z. G. Zang, X. X. Liu, B. C. Li, Z. Y. Xiao, S. R. Lu, H. Gong, J. Y. Ouyang and K. Sun, *J Mater Chem A*, 2018, **6**, 16583-16589.
5. Y. Zhu, S. Wang, R. X. Ma and C. Y. Wang, *Sol Energy*, 2019, **188**, 28-34.
6. S. Shahbazi, F. Tajabadi, H. S. Shiu, R. Sedighi, E. Jokar, S. Gholipour, N. Taghavinia, S. Afshar and E. W. G. Diau, *Rsc Adv*, 2016, **6**, 65594-65599.
7. D. Huang, T. Goh, J. Kong, Y. F. Zheng, S. L. Zhao, Z. Xu and A. D. Taylor, *Nanoscale*, 2017, **9**, 4236-4243.
8. W. B. Han, G. H. Ren, J. M. Liu, Z. Q. Li, H. C. Bao, C. Y. Liu and W. B. Guo, *Acs Appl Mater Inter*, 2020, **12**, 49297-49322.
9. J. Tirado, M. Vasquez-Montoya, C. Roldan-Carmona, M. Ralairisoa, N. Koch, M. K. Nazeeruddin and F. Jaramillo, *Acs Appl Energ Mater*, 2019, **2**, 4890-4899.
10. Y. Diao, Y. Lu, H. Yang, H. Wang, H. Chen and J. M. D'Arcy, *Adv Funct Mater*, 2020, **30**, 2003394.
11. Y. Diao, H. Chen, Y. Lu, L. M. Santino, H. Wang and J. M. D'Arcy, *Acs Appl Energ Mater*, 2019, **2**, 3435-3444.
12. D. M. Niedzwiedzki, T. Tronina, H. Liu, H. Staleva, J. Komenda, R. Sobotka, R. E. Blankenship and T. Polivka, *Biochimica et Biophysica Acta (BBA)-Bioenergetics*, 2016, **1857**, 1430-1439.
13. I. H. van Stokkum, D. S. Larsen and R. van Grondelle, *BBA-Bioenergetics*, 2004, **1657**, 82-104.
14. R. Sheng, A. Ho-Baillie, S. J. Huang, S. Chen, X. M. Wen, X. J. Hao and M. A. Green, *J Phys Chem C*, 2015, **119**, 3545-3549.
15. B. Wenger, P. K. Nayak, X. M. Wen, S. V. Kesava, N. K. Noel and H. J. Snaith, *Nat Commun*, 2017, **8**.
16. Y. Yang, Y. Yan, M. J. Yang, S. Choi, K. Zhu, J. M. Luther and M. C. Beard, *Nat Commun*, 2015, **6**.
17. R. J. Elliott, *Phys Rev*, 1957, **108**, 1384-1389.
18. J. J. Shi, H. Y. Zhang, Y. M. Li, J. J. Jasieniak, Y. S. Li, H. J. Wu, Y. H. Luo, D. M. Li and Q. B. Meng, *Energ Environ Sci*, 2018, **11**, 1460-1469.
19. C. L. Davies, M. R. Filip, J. B. Patel, T. W. Crothers, C. Verdi, A. D. Wright, R. L. Milot, F. Giustino, M. B. Johnston and L. M. Herz, *Nat Commun*, 2018, **9**.
20. M. Saba, M. Cadelano, D. Marongiu, F. P. Chen, V. Sarritzu, N. Sestu, C. Figus, M. Aresti, R. Piras, A. G. Lehmann, C. Cannas, A. Musinu, F. Quochi, A. Mura and G. Bongiovanni, *Nat Commun*, 2014, **5**.
21. Y. Yamada, T. Nakamura, M. Endo, A. Wakamiya and Y. Kanemitsu, *Ieee J Photovolt*, 2015, **5**, 401-405.
22. J. Even, L. Pedesseau and C. Katan, *J Phys Chem C*, 2014, **118**, 11566-11572.
23. Q. Q. Lin, A. Armin, R. C. R. Nagiri, P. L. Burn and P. Meredith, *Nat Photonics*, 2015, **9**, 106-112.
24. F. Rut, L. F. Ayguler, N. Giesbrecht, B. Rendenbach, A. Magin, P. Docampo, H. Kait and M. Hetterich, *Apl Mater*, 2019, **7**.
25. N. Sestu, M. Cadelano, V. Sarritzu, F. P. Chen, D. Marongiu, R. Piras, M. Mainas, F. Quochi, M. Saba, A. Mura and G. Bongiovanni, *J Phys Chem Lett*, 2015, **6**, 4566-4572.
26. R. Comin, G. Walters, E. S. Thibau, O. Voznyy, Z. H. Lu and E. H. Sargent, *J Mater Chem C*, 2015, **3**, 9480-9480.
27. I. B. Koutselas, L. Ducasse and G. C. Papavassiliou, *J Phys-Condens Mat*, 1996, **8**, 5953-5953.
28. Y. Jiang, X. Wang and A. L. Pan, *Adv Mater*, 2019, **31**.
29. M. Baranowski and P. Plochocka, *Adv Energy Mater*, 2020, **10**.

30. J. S. Manser, J. A. Christians and P. V. Kamat, *Chem Rev*, 2016, **116**, 12956-13008.
31. I. Robel, B. A. Bunker, P. V. Kamat and M. Kuno, *Nano Lett*, 2006, **6**, 1344-1349.
32. P. Piatkowski, B. Cohen, F. J. Ramos, M. Di Nunzio, M. K. Nazeeruddin, M. Gratzel, S. Ahmad and A. Douhal, *Phys Chem Chem Phys*, 2015, **17**, 14674-14684.
33. J. S. Manser and P. V. Kamat, *Nat Photonics*, 2014, **8**, 737-743.
34. S. D. Stranks, V. M. Burlakov, T. Leijtens, J. M. Ball, A. Goriely and H. J. Snaith, *Phys Rev Appl*, 2014, **2**.
35. V. S. Chirvony, K. S. Sekerbayev, H. P. Adl, I. Suarez, Y. T. Taurbayev, A. F. Gualdrón-Reyes, I. Mora-Sero and J. P. Martínez-Pastor, *J Lumin*, 2020, **221**.
36. S. D. Stranks, G. E. Eperon, G. Grancini, C. Menelaou, M. J. Alcocer, T. Leijtens, L. M. Herz, A. Petrozza and H. J. Snaith, *Science*, 2013, **342**, 341-344.
37. Q. L. Bao, H. Zhang, Y. Wang, Z. H. Ni, Y. L. Yan, Z. X. Shen, K. P. Loh and D. Y. Tang, *Adv Funct Mater*, 2009, **19**, 3077-3083.
38. J. H. Espenson, McGraw-Hill Book Company, New York, 1981, p. p. 35.
39. C. Wehrenfennig, G. E. Eperon, M. B. Johnston, H. J. Snaith and L. M. Herz, *Adv Mater*, 2014, **26**, 1584-1589.
40. Y. Yang, M. J. Yang, Z. Li, R. Crisp, K. Zhu and M. C. Beard, *J Phys Chem Lett*, 2015, **6**, 4688-4692.
41. E. Burstein, *Phys Rev*, 1954, **93**, 632-633.
42. T. S. Moss, *P Phys Soc Lond B*, 1954, **67**, 775-782.
43. A. Miyata, A. Mitioglu, P. Plochocka, O. Portugall, J. T. W. Wang, S. D. Stranks, H. J. Snaith and R. J. Nicholas, *Nat Phys*, 2015, **11**, 582-U594.
44. K. Tanaka, T. Takahashi, T. Ban, T. Kondo, K. Uchida and N. Miura, *Solid State Commun*, 2003, **127**, 619-623.
45. N. Massonnet, A. Carella, O. Jaudouin, P. Rannou, G. Laval, C. Celle and J. P. Simonato, *J Mater Chem C*, 2014, **2**, 1278-1283.
46. H. J. Ahonen, J. Lukkari and J. Kankare, *Macromolecules*, 2000, **33**, 6787-6793.
47. I. Zozoulenko, A. Singh, S. K. Singh, V. Gueskine, X. Crispin and M. Berggren, *ACS Applied Polymer Materials*, 2019, **1**, 83-94.
48. J. L. Bredas and G. B. Street, *Accounts Chem Res*, 1985, **18**, 309-315.
49. E. Serpetzoglou, I. Konidakis, G. Kakavelakis, T. Maksudov, E. Kymakis and E. Stratakis, *ACS Appl Mater Interfaces*, 2017, **9**, 43910-43919.
50. K. Ishioka, B. G. Barker, M. Yanagida, Y. Shirai and K. Miyano, *J Phys Chem Lett*, 2017, **8**, 3902-3907.
51. E. Ugur, J. I. Khan, E. Aydin, M. C. Wang, M. Kirkus, M. Neophytou, I. McCulloch, S. De Wolf and F. Laquai, *J Phys Chem Lett*, 2019, **10**, 6921-6928.
52. J. C. Brauer, Y. H. Lee, M. K. Nazeeruddin and N. Banerji, *J Phys Chem Lett*, 2015, **6**, 3675-3681.
53. F. Wang, J. Shan, M. A. Islam, I. P. Herman, M. Bonn and T. F. Heinz, *Nat Mater*, 2006, **5**, 861-864.
54. W. Liptay, in *Excited States*, ed. E. C. Lim, Academic Press, New York, 1974, vol. 1, pp. 129-229.
55. A. Sacra, D. J. Norris, C. B. Murray and M. G. Bawendi, *J Chem Phys*, 1995, **103**, 5236-5245.
56. C. S. Ponseca, E. M. Hutter, P. Piatkowski, B. Cohen, T. Pascher, A. Douhal, A. Yartsev, V. Sundstrom and T. J. Savenije, *J Am Chem Soc*, 2015, **137**, 16043-16048.
57. J. Leng, J. X. Liu, J. Zhang and S. Y. Jin, *J Phys Chem Lett*, 2016, **7**, 5056-5061.